Flexible Electronics and Materials for Synchronized Stimulation and Monitoring in Multi-Encephalic Regions

Wei Ling, Jingxian Yu, Ning Ma, Ya Li, Ziyue Wu, Rong Liang, Yafeng Hao, Huizhuo Pan, Wentao Liu, Bo Fu, Kun Wang, Hanjie Wang, Lizhu Li, Xing Sheng, Hui Peng, Baoan Ning, Jiajia Yang, and Xian Huang*

Simultaneous neuron stimulation and biophysiological sensing in multi-encephalic regions can lead to profound understanding of neural pathways, neurotransmitter transportation, and nutrient metabolism. Here, a flexible electronic device with tentacle-like channels radiating from a central wireless circuit is presented. The device is constructed by different organic and inorganic materials that have been made into thin-film or nanoparticle formats. All channels have been equipped with flexible components for distributed and synchronized opto-electrical stimulation, biopotential sensing, and ion concentration monitoring. They can be implanted into different brain regions through adaptive bending and individually addressed to follow programmable working sequences. Experimental results conducted in vitro and in vivo have demonstrated the capability in generating optical or electrical stimulation, while sensing 16-channels biopotential and concentration of Ca^{2+}, Na^+, and K^+ ions in distributed regions. Behavior and immunohistochemistry studies suggest potential applications in regulating brain functions for freely moving animals. In combination with various functional materials, the device can serve as a comprehensive research platform that can be modularized to accommodate different needs for brain studies, offering numerous possibilities and combinations to yield sophisticated neuromodulation and behavior regulation.

1. Introduction

The human brain contains more than 80 billion neurons scattered within different brain regions that vary in neural structures, chemistry, and connectivity.[1–5] Physical and chemical signal transmitted within these regions is governed locally by synapses among neurons and projected regionally by neural pathways that include some notable paths such as arcuate fasciculus[6] and retinohypothalamic tract[7] as well as

many undiscovered patterns. Efforts in revealing the mystery of brains have led to the appearance of many neurological devices include silicon-based microneedle arrays,[8–10] glass pipette-mounted devices,[11,12] and high-density microelectrode arrays[13,14] that contain rigid fibers or electrodes driven by passive or active electronic matrixes. However, these devices are mechanically incompatible with soft and curvilinear brain tissues, and, thus, unable to achieve intimate tissue contact with minimized damage.

To tackle the issues of effective interfacing with brain tissues, flexible electronics technology has been used to develop devices such as battery-free injectable opto-fluidic microsystems,[15,16] bioresorbable photonic devices,[17,18] and injectable electronic meshes.[19–21] Despite innovative designs and working mechanisms, the majority of these flexible neurological devices cannot perform simultaneous stimulation and sensing among multi-encephalic regions. Therefore, flexible electronics that can achieve comprehensive functions such as optogenetics,[22,23] deep brain stimulation,[24,25] neural electrophysiology,[26] and chemical monitoring[27,28] within distributed areas are still highly demanded. However, the achievement of the above functions demands highly stable and consistent electronic multi-channels equipped with various flexible components. Such kinds of flexible electronics have been rarely reported not to mention the demonstration of their practical applications in neurology.

W. Ling, J. Yu, Y. Li, Z. Wu, Prof. J. Yang, Prof. X. Huang
Department of Biomedical Engineering
Tianjin University
92 Weijin Road, Tianjin 300072, China
E-mail: huangxian@tju.edu.cn
N. Ma, Y. Hao, H. Pan, Prof. H. Wang
Department of Life Science
Tianjin University
92 Weijin Road, Tianjin 300072, China

The ORCID identification number(s) for the author(s) of this article can be found under https://doi.org/10.1002/adfm.202002644.

R. Liang
Academy of Medical Engineering and Translational Medicine
Tianjin University
92 Weijin Road, Tianjin 300072, China
W. Liu, Dr. B. Fu, K. Wang, Prof. H. Peng, Prof. B. Ning
Tianjin Institute of Environmental and Operational Medicine
1 Dali Road, Tianjin 300050, China
L. Li, Prof. X. Sheng
Department of Electronic Engineering
Tsinghua University
Beijing 100084, China

2002644 (1 of 13)

**ADVANCED
SCIENCE NEWS**
www.advancedsciencenews.com

**ADVANCED
FUNCTIONAL
MATERIALS**
www.afm-journal.de

Here, we present a flexible implantable device with multiple scattered channels radiated from a central wireless circuit. The device is constructed by various organic and inorganic materials that have been made into thin-film and nanoparticle formats, and is inspired by the brain/tentacle configurations of octopuses that use the central brain to process the signal from sensory organs in their tentacles. The flexible channels can be adaptively bent to accommodate different distances to the multi-encephalic regions. Each of the channels contains a blue micro light-emitting diode (μ-LED), four biopotential electrodes, and three ion-selective sensors, allowing the performance of distributed, programmable opto-electrical stimulations, and synchronous sensing of resulting biophysiological response. Recording of electrical and chemical signal evoked by in situ optical or electrical stimulation has been demonstrated, followed by further demonstration of the neuromodulation on freely moving animals through behavior studies. Furthermore, the immunohistochemistry results reveal that the channels are biocompatible to brain tissue and are suitable for long-term implantable applications. The proposed device represents an emerging type of flexible electronics that features multiple electronic tentacles to access different organs or locations.[28] The numbers of channels and functional components on this comprehensive platform are expandable for higher spatial resolution and more sophisticated assignments to facilitate brain–computer interface, trans-species communication, and in-depth understanding of brain mechanisms.

2. Results

2.1. Design and Fabrication of the Multichannel Implantable Device

The schematics and the concept of a flexible electronic device with four tentacle-like channels scattered from a central wireless circuit have been demonstrated in **Figure 1**a. The four channels can be implanted into different brain regions of a rat, and conduct optical stimulation at specific wavelengths, while monitoring neural response such as action potential and ionic concentrations. Each of the channels contains two stacked polyimide (PI) substrates equipped with a μ-LED for optogenetic stimulation, four microelectrodes for biopotential monitoring and stimulation, and three ion-selective sensors to monitor Ca^{2+}, Na^+, and K^+. The exploded illustration in Figure 1b shows stacked multi-layers of a single channel whose detailed fabrication processes have been shown in Figure S1, Supporting Information, and Experimental Section. The μ-LED ($190 \times 110 \times 8$ μm^3) (Figure 1c) was released from a sapphire substrate and transfer-printed onto the upper PI substrate. The μ-LED can be coated with either cadmium selenide (CdSe)/zinc sulfide (ZnS) quantum dots or phosphors to achieve other emission wavelengths. Four microelectrodes (30 μm in diameter) formed by Ti/Cu/Ti/Au multi-layers are aligned parallelly to each other, enclosing the μ-LED in the center (Figure 1d). They can be surface-modified with gold nanoparticles (AuNPs) to reduce contact impedance during the measurement. The three ion-selective sensors that are located on the lower PI substrate contain three working electrodes and one shared reference

electrode. The working electrodes are modified with K^+/Na^+/Ca^{2+} selective membranes and coated with poly(3,4-ethylenedioxythiophene) polystyrene sulfonate (PEDOT:PSS) for ion-to-electron transduction. The reference electrode is modified with polyvinyl butyral (PVB)/sodium chloride (NaCl) solid electrolyte to minimize the potential drift. The resulting channel has an overall dimension of 600 μm × 2 cm × 80 μm with a sharp tip to facilitate implantation (Figure S2, Supporting Information).

A wireless circuit (Figure 1e; Figure S3, Supporting Information) synchronizes the working sequences of all channels and processes the corresponding signal, allowing programmable light stimulation (Figure 1f; Video S1, Supporting Information) and sensing. All channels can be bent to adapt to implantation locations with minimized damage to the brain, while the wireless circuit can be readily mounted onto the skull (Figure 1g). When powered by a lithium-ion battery, the entire system can wirelessly regulate and monitor neural activity on freely moving animals without interfering their behaviors (Video S2, Supporting Information). Different wireless circuits that have been developed in corresponding to the modularized functions of the channels offer different levels of complexity and the resulting weights. For example, circuits for wireless optical stimulation and wireless ion monitoring weighted 1.48 and 2.29 g, respectively (Figure S4, Supporting Information).

2.2. Characterization of μ-LEDs

The μ-LEDs in the channels were first characterized to reveal their performance in thin-film formats. Ultrathin μ-LEDs were released from patterned sapphire substrates through a laser lift-off process, resulting in a thickness of ≈8 μm (**Figure 2**a; Figure S5, Supporting Information). Partial decomposition of the gallium nitride (GaN) layer during the lift-off process may lead to reduced charge carriers in the PN junction. As a result, current under the same applied voltage has been reduced after laser lift-off (Figure S6a, Supporting Information). In addition, the emission wavelength of the μ-LEDs has been observed to shift from 469 to 472 nm after transfer printing and integrating on the channel (Figure 2b). The shift in emission wavelength may be attributed to the covering PI layer. However, the shifted wavelength still complies with the activation wavelength of the channelrhodopsin-2 (ChR2).[29] By coating CdSe/ZnS quantum dots or phosphors onto the blue μ-LED, emission colors of orange (592 nm, Figure 2c), green (523 nm, Figure S6b, Supporting Information), and red (624 nm, Figure S6c, Supporting Information) can be readily achieved to activate different photoreceptors in optogenetics.[30,31] The optical power density of the channel was measured to be 6.53 mW mm^{-2} at an input current of 0.5 mA (Figure 2d). With a higher input current of 3 mA, the optical power density can reach 35.11 mW mm^{-2}, offering the capacity to stimulate larger cell populations. The light transmission was then evaluated using brain slices with thicknesses ranging from 0.5 to 3 mm (Figure S7, Supporting Information). The transmitted power through a 1-mm-thick slice maintained at a range from 23.91% to 26.97% (Figure S8a, Supporting Information) when the input current changed from 0.2 to 2 mA. Besides, the transmitted power of the light changed monotonously from 45.66% to 3.96% when the slice
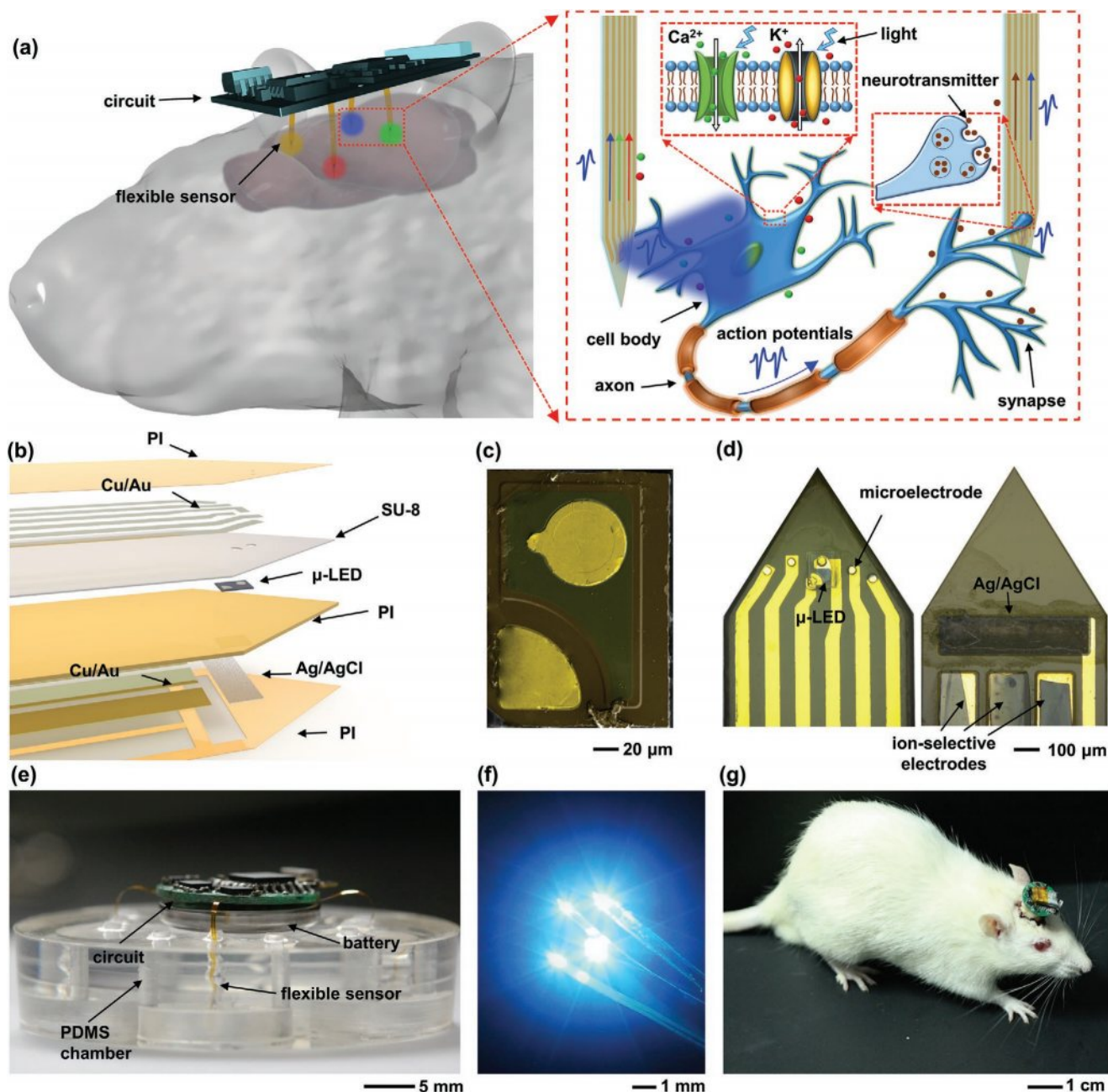
Figure 1. Flexible electronic devices for stimulating and monitoring in multi-encephalic regions. a) A schematic of an implantable flexible device that offers opto-electrical stimulation and biophysiological sensing using scattered multiple channels. b) The exploded view of a single flexible channel that contains a μ-LED, four microelectrodes, and three ion-selective sensors. c) A colorized SEM image of the μ-LED after lifting off by laser. d) Images of the top and bottom sides of an implanted channel. e) An image of a wireless circuit connected with four channels that have been inserted into a PDMS chamber. f) An image of four working channels whose μ-LEDs have been turned on. g) An image of a freely moving rat that has been implanted with a flexible device.

thicknesses varied from 0.5 to 3 mm (Figure S8b, Supporting Information). According to the fitting result of Figure S8b, Supporting Information, and the measurement result of Figure 2d, the transmission at 0.3 mm tissue thickness is 53% and the emission power at 2 mA is 0.66 mW from the μ-LEDs. Thus, the power density of the μ-LEDs after penetrating through a 0.3 mm tissue at a 120° emission angle can be determined to be 1.24 mW mm^{-2} that is larger than the required power density (1 mW mm^{-2})[32] for activating the photoreceptors. In our future research, it is feasible to use μ-LEDs with higher wall-plug efficiency (>70%) as compared with 13% for current μ-LEDs, allowing even larger penetration depth and less power consumption.

The mechanical and thermal characteristics of the μ-LEDs were further studied. When the channel was subject to bending with a radius of ≈1 cm, the current-voltage curves of
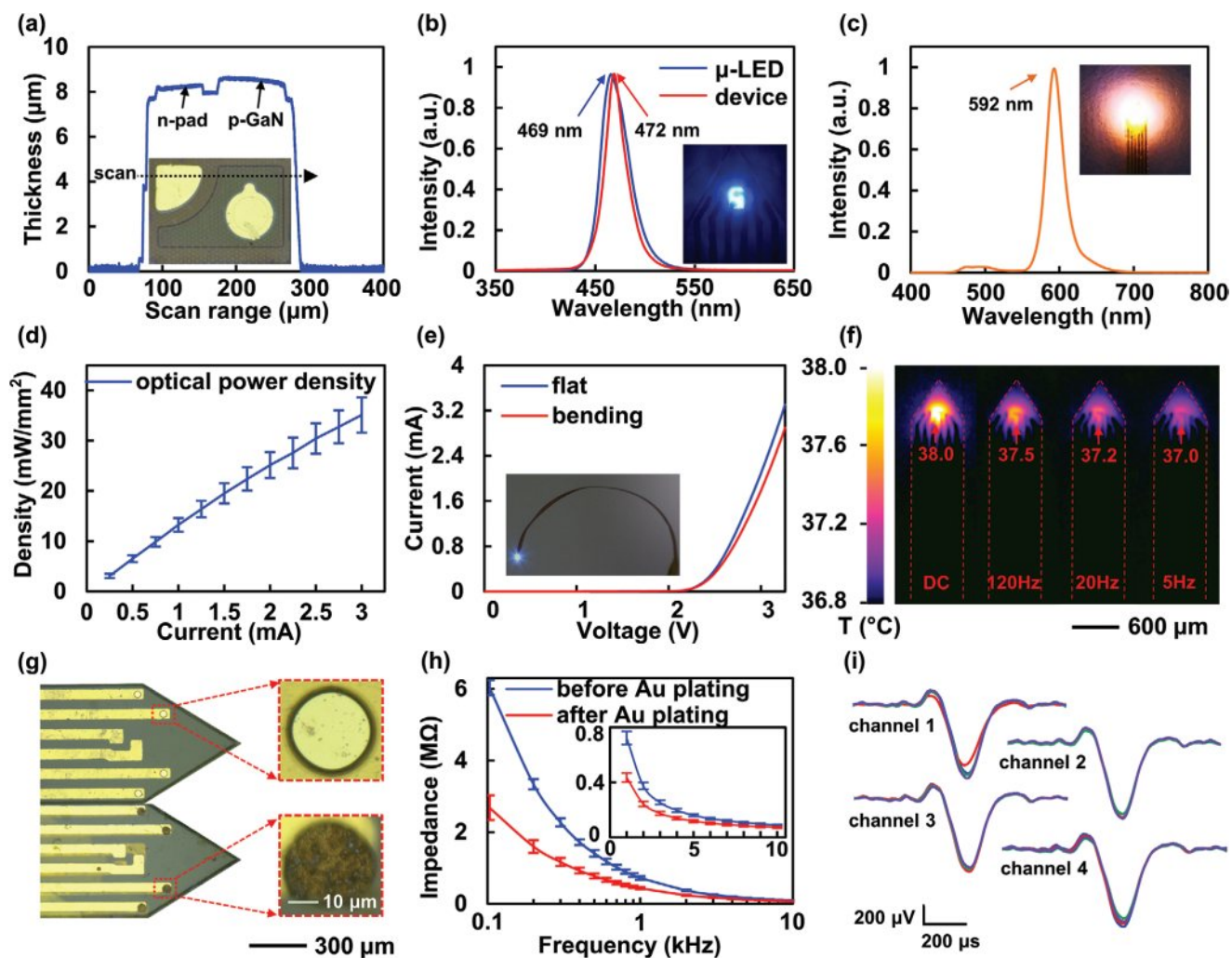
Figure 2. Characterization of μ-LEDs and microelectrodes in the flexible device. a) Surface profile of a μ-LED after lifting off by laser. The electroluminescent spectra for μ-LEDs b) before and c) after coating with CdSe/ZnS quantum dots. d) Optical power density as a function of electrical input current. $n = 4$, error bars indicate means ± SD. e) Current–voltage characteristics of μ-LEDs with and without bending. f) Measured temperature distribution of a channel of the device under different frequencies of the driving voltage. g) Images of planar Au electrodes and AuNPs-modified electrodes. h) Impedance measurements of micro-electrodes before and after AuNPs modification. $n = 4$, error bars indicate means ± SD. i) Measured signal spikes of 16 electrodes in 4 channels.

the μ-LEDs were almost unchanged as compared with the flat channel (Figure 2e). The fatigue test by repeatedly bending the channel for 500 cycles also suggests no significant performance degradation (Figure S9, Supporting Information), indicating the excellent mechanical property of the channel in withstanding external stress. The thermal effect of the μ-LEDs was characterized under direct current (DC) and alternating current (AC) driving voltages on a hotplate maintained at 37 °C (Figure 2f). The temperature increase was 1 °C under a DC voltage of 2.6 V, while the temperature changes were less than 0.5 °C when μ-LEDs blinked at 5, 20, and 120 Hz with 5 ms pulse width under an AC voltage of 2.6 V. The thermal energy generated by the μ-LED was dissipated rapidly to the periphery through the underlying heat-dissipating Cu layer. Besides, the brain tissue may also help to dissipate thermal energy via thermal conduction and blood perfusion. Better heat dissipation can be achieved by depositing a thicker

Cu layer or using other heat-dissipating materials with better thermal conductivity such as graphite or graphene.

2.3. Characterization of Microelectrodes

The interfacing impedance between the microelectrodes and the surrounding liquid was reduced to enhance the fidelity of the neural signal recording.[33] Electroplating AuNPs onto the electrodes (Figure 2g) results in a 39.8% decrease in the impedance of the electrodes at 1 kHz as compared with the bare electrodes (Figure 2h). The electrodes also showed enhanced electrochemical behaviors after coating with AuNPs. The cyclic voltammetry curve of the AuNPs-modified electrode exhibits a highly faradic behavior in corresponding to a much larger elliptical shape than the bare electrode (Figure S10, Supporting Information), indicating improved charge storage capacity and charge transfer

efficiency during electrophysiological recording. Four flexible channels (Figure S11a, Supporting Information) were then immersed into the artificial cerebral spinal fluid (ACSF) with an additional channel connected to a signal generator that supplied simulated spikes (Figure S11b, Supporting Information). The signal recorded by all electrodes on the channels shows high consistency in shapes with slight variation in amplitudes due to the difference in electrode impedance (Figure 2i). The characterization results indicate low interfacing impedance to the surrounding environment and high signal consistency among different electrodes, suggesting promising use of the microelectrode arrays in in vivo biopotential mapping.

2.4. Characterization of Ion-Selective Sensors

The chemical sensing capability of the system has been demonstrated by monitoring concentrations of ions that are vital for neuromodulation and behavior control.[34] The characterization of each sensor was performed individually using different

electrolyte solutions. The sensors in the corresponding electrolyte solutions exhibit linear response with increasing concentrations of K^+, Na^+, and Ca^{2+} (**Figure 3**a–c). The sensitivities were calculated to be 64.7, 82.1, and 34.8 mV per decade of concentration for K^+, Na^+, and Ca^{2+} sensors, respectively. Considering the actual levels of ions in the cerebrospinal fluid (2.5–3.2 mм for K^+, 136–150 mм for Na^+, and 1–1.5 mм for Ca^{2+}),[35] the sensing ranges of the presented sensors are suitable for implantable applications. Reversibility of the sensors was tested by repeatedly changing the ions from low to high concentrations for three times. The results indicate small signal drift of less than 5, 8, and 22 μV, respectively for Ca^{2+} (Figure 3d), K^+ (Figure S12a, Supporting Information), and Na^+ (Figure S12b, Supporting Information) sensors after three cycles. The selectivity of the Ca^{2+} sensor was determined by adding interfering analytes (e.g., Mg^{2+}, K^+, Na^+) in sequence. Only Na^+ ions induced a slight response that is ≈4.5 times smaller than Ca^{2+} sensing, while other ions showed negligible interference (Figure 3e). The K^+ and Na^+ sensors also possessed excellent selectivity to the target electrolytes with the presence
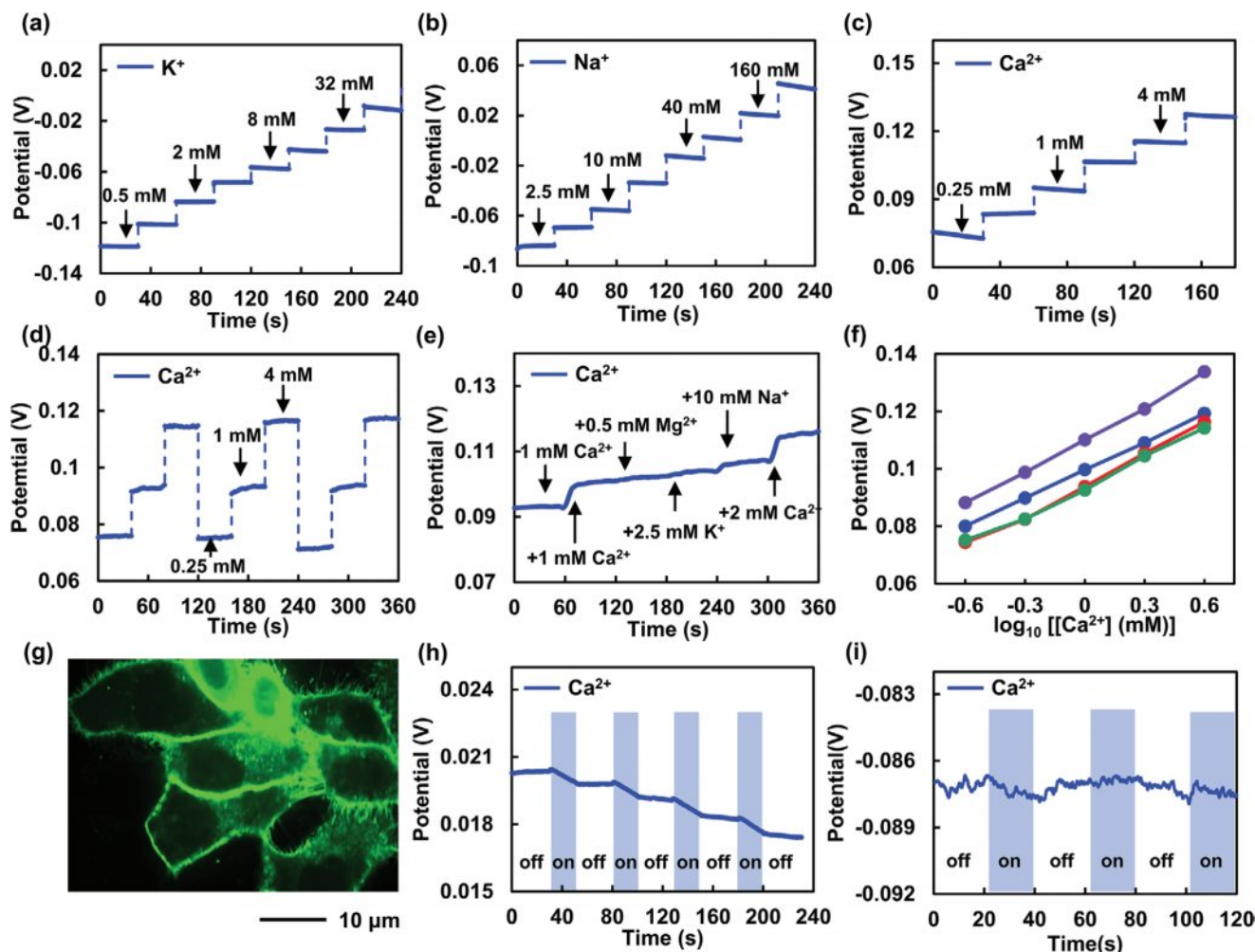
Figure 3. Characterization of ion-selective sensors. The response of the open-circuit potential of the a) K^+, b) Na^+, and c) Ca^{2+} sensors in KCl, NaCl, and $CaCl_2$ solutions. d) Reversibility and e) selectivity of the Ca^{2+} sensor. f) The difference in the sensor response of four Ca^{2+} sensors. g) A fluorescent image of 293T cells transfected by plasmid *pcDNA3.1/ChR2-GFP*. The response of the open-circuit potential of a Ca^{2+} sensor to the light stimulation in solutions h) with and i) without transfected cells.

of other interferences (Figure S12c,d, Supporting Information). Sensor variation due to fabrication errors has been determined using four sensors for each kind of ions. The Ca^{2+} sensors show sensitivity ranging from 32.6 to 37.8 mV per decade of concentration with a relative standard deviation (RSD) of 5.87% (Figure 3f). Similarly, the RSDs for the K^+ sensors and the Na^+ sensors are both less than 3.5%. The sensitivity ranges are 61.5–66.7 and 78.2–86.3 mV per decade of concentration for the K^+ sensors (Figure S12e, Supporting Information) and the Na^+ sensors (Figure S12f, Supporting Information), respectively. The variation among sensors can be tackled by a pre-calibration process for each sensor to further minimize the sensing errors among sensors on different channels. The characterization results of the ion-selective sensors indicate high selectivity and reversibility in chemical detection, suggesting favorable performance for the complex brain environment.

Sensor performance in response to ion concentration changes in optogenetics has been selectively demonstrated using Ca^{2+} due to its vital role as the second messenger in many cellular functions.[36] The μ-LED was used to stimulate 293T cells, which were transfected with pcDNA3.1-based plasmids that delivered ChR2 fused to the green fluorescent protein (*pcDNA3.1/ChR2-GFP*, Figure 3g). Decreased open-circuit potential of the sensor can be observed with optical stimulation (Figure 3h), indicating reduced Ca^{2+} concentration caused by the influx of environmental Ca^{2+} into cells due to the opening of the light-gated Ca^{2+} channels within the cell membranes. As a comparison, the sensor was dipped into an ACSF solution without transfected 293T cells. The sensor showed negligible responses to the optical stimulation (Figure 3i), indicating that the change in potential in Figure 3h was not caused by the interfering photoelectric effect. The results demonstrate that the ion-selective sensors can coordinate with optogenetic devices to monitor the effectiveness of optical stimulation to the ion channels.

2.5. Multichannel In Vivo Electrophysiological Recording and Ca^{2+} Monitoring

The device has been demonstrated to conduct multichannel recording of neural activities in response to opto-electrical stimulation. Four flexible channels have been implanted into four brain areas (e.g., deep gray layer of the superior colliculus [DpG], anteroventral thalamic nucleus [AV], caudate putamen [Cpu], and ventral hippocampus [vHPC] with the help of a stereotaxic apparatus) (**Figure 4**a). Local field potential (LFP) that reflected the dynamic flow of neuronal information across the brain was obtained by filtering the raw signal with a low-pass cutoff frequency of 300 Hz and negligible noises of ±18 μV (Figure 4b), suggesting feasibility to use the device for correlation analysis and projection mapping between multiple brain areas. The power spectra showed that the LFP signal mainly concentrated in low frequencies (<50 Hz) (Figure S13, Supporting Information), indicating that the recorded signal may arise from the summation of excitatory and inhibitory dendritic potential from the surrounding neurons. Spontaneous spike signal can be further obtained by filtering the raw signal with a band-pass frequency from 500 to 5000 Hz (Figure 4c) and sorting

with principal component analysis (Figure 4d; Figure S14, Supporting Information). The results indicate three different spikes that may be generated by three surrounding neurons. The maximum signal-to-noise ratio was calculated to be 8.1, which compared better than other reported electrodes.[10,19,20] A microelectrode was then used reversely to generate electrical stimulation, and the rest of the microelectrodes continuously monitored the response signal. Evoked action potential has been detected in vHPC during 25 Hz electrical stimulation with short latencies of ≈10 ms (Figure S15, Supporting Information). The results of biopotential monitoring indicate the device's capability in mapping both spontaneous and evoked neural activities in multi-encephalic regions.

In vivo Ca^{2+} measurement combining with optogenetics was then performed. Rats were transfected in the medial prefrontal cortex (mPFC) with *AAV9-CaMKIIα::hChR2-eYFP*, which is an adeno-associated virus (AAV9) expressing hChR2 fused to the enhanced yellow fluorescent protein (eYFP) under the control of calmodulin kinase II α-subunit (CaMKIIα) promoter. Flexible channels were then implanted into the mPFC of rats, which have been successfully transfected with the virus according to the fluorescence images of mPFC slices obtained after completion of the experiments (Figure 4e). Reversible Ca^{2+} concentrations can be observed during repeated optical stimulation (Figure 4f). The decrease in Ca^{2+} concentration can be attributed to the influx of Ca^{2+} into the neurons as described above, while the rapid recovery may be due to the self-regulating ability of the extracellular environment. Despite that the sensitivity for ion monitoring under light regulation and the stability for long-term monitoring need further exploration, the obtained results reveal that the device can be used to record changes in ion concentration during in vivo optogenetics, offering novel approaches to evaluate the effectiveness of neuromodulation. In addition to the ion concentration measurement, the electrochemical sensors can be readily modified to monitor other chemicals such as neurotransmitters, glucose, and cortisol that may be related to various biological processes in the brain.

2.6. Electrophysiological Recording of Projection Dynamics

Multi-encephalic electrophysiological recording with programmable optical stimulation was presented for neural projection mapping. Rats were injected with *AAV9-CaMKIIα::hChR2-eYFP* in the basolateral amygdala (BLA) of the right hemisphere and were allowed to recover for at least one month. Two channels were then implanted into the BLA in both hemispheres (**Figure 5**a). Long light pulse (500 ms) was used to minimize the photoelectric artifact in the measured neural potential. Light-modulated signal can be observed in the transfected BLA (Figure 5b), while the channel implanted in the other hemisphere showed no response (Figure S16, Supporting Information). The power spectral density (PSD, Figure 5d) that indicates intense neural activity during the periods of light stimulation as compared with the dark periods suggests successful activation of photoreceptors and corresponding neurons. An additional channel was further implanted into the
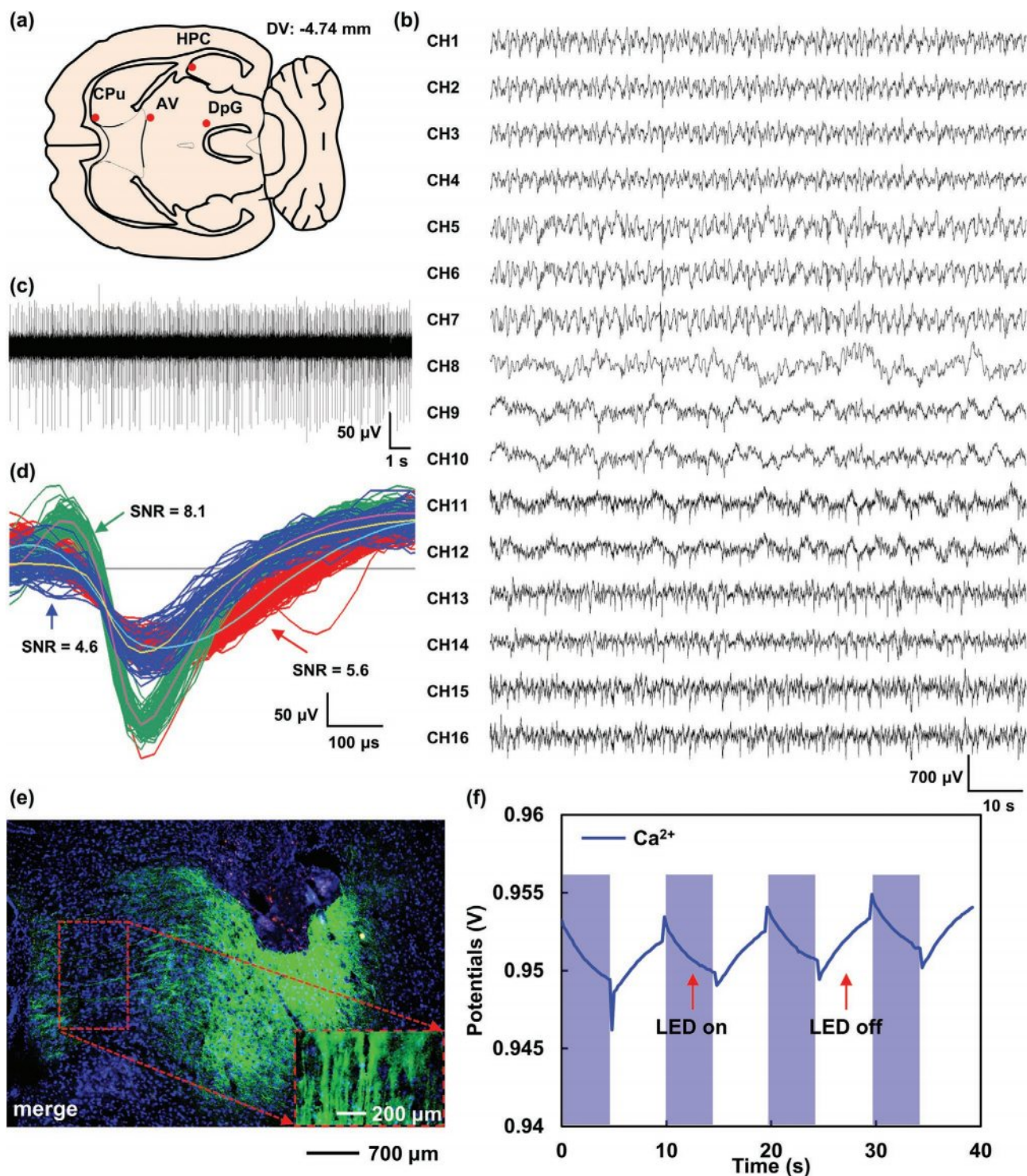
ADVANCED
SCIENCE NEWS
www.advancedsciencenews.com

ADVANCED
FUNCTIONAL
MATERIALS
www.afm-journal.de

Figure 4. In vivo electrophysiological recording and Ca^{2+} monitoring. a) An illustration of four brain areas where the simultaneous electrical recording was conducted. b) 16-channel LFPs data (60 s) recorded from the four brain areas. CH1-4: DpG. CH5-8: AV. CH9-12: Cpu. CH13-16: vHPC. c) Spontaneous extracellular spikes recorded in the vHPC. d) Averaged and sorted spikes using the principal component analysis to identify individual units. e) A fluorescence image of mPFC slices transfected with *AAV9-CaMKIIα::hChR2-eYFP*. f) Change of the open-circuit potential of a Ca^{2+} sensor during the process of optical stimulation in the mPFC.

vHPC that is known as a projection target from the BLA[37] to conduct the study of neural circuit mapping (Figure 5a). Light generated in the vHPC can excite axons extended from neu-

rons in the BLA, resulting in evoked spikes generated from the neurons in the BLA and cascaded neural reaction in the vHPC. As a result, evoked spikes can also be detected by the
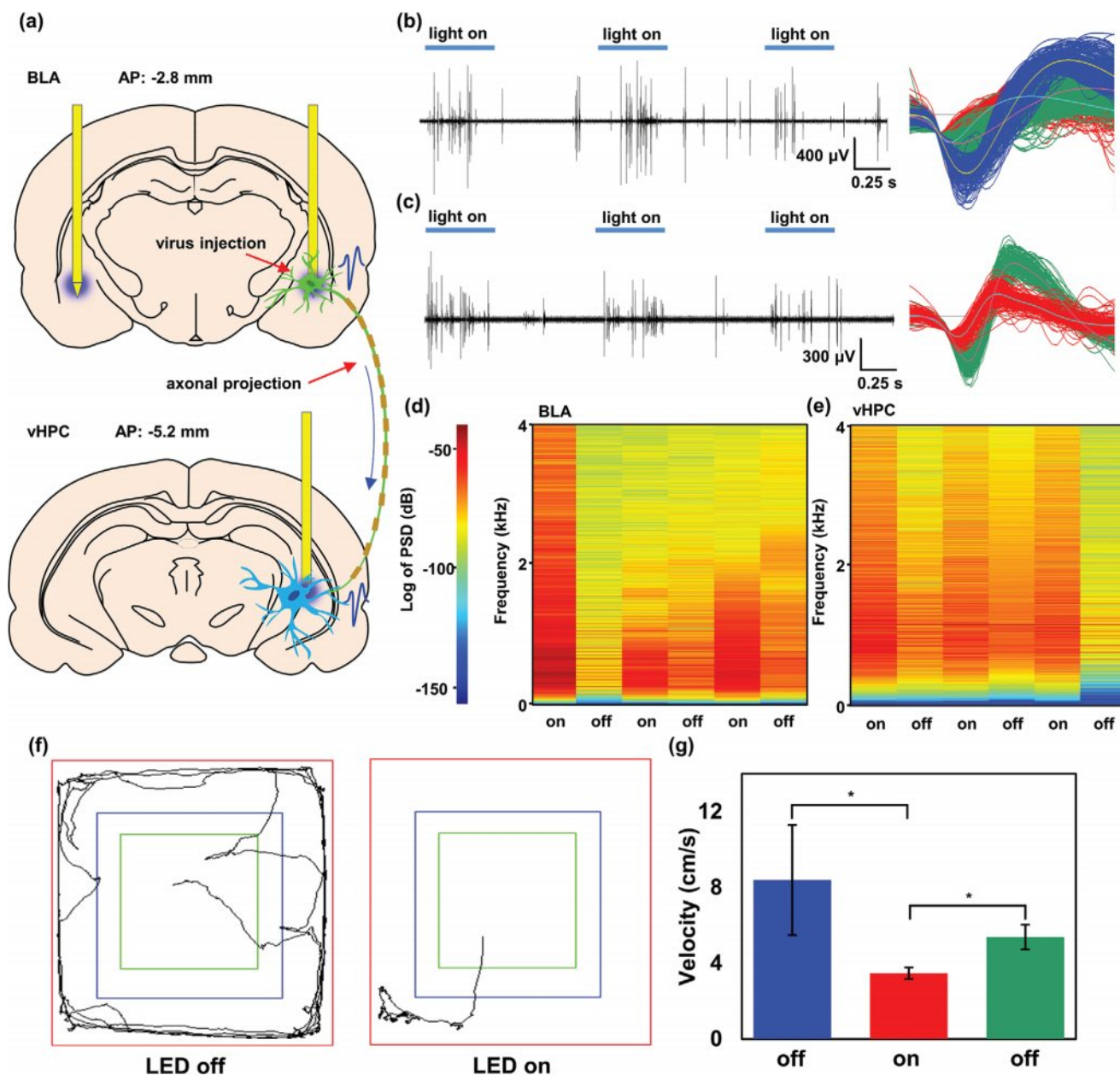
Figure 5. Optogenetic projection mapping and behavior study. a) An illustration of virus injection, optical stimulation, and electrical recording in the BLA and the BLA-to-vHPC projection. b) Left: Evoked action potential after the light stimulation in the BLA. Right: Averaged shapes of the action potential. c) Left: Evoked action potential from the BLA-to-vHPC projection. Right: Averaged shapes of the action potential. Power spectral density of the recorded signal in the d) BLA and e) vHPC during optogenetic stimulation. f) Representative traces of movement from the same rat in OFT without and with optical stimulation. g) The average velocity in OFT for rats with or without the optical stimulation in the LHb. $n = 3$, error bars indicate means $\pm$ SD. $*p < 0.05$, paired Student's t-test.

microelectrodes within the vHPC (Figure 5c). Again, PSD result suggests intense neural activity in the vHPC due to the excitation signal transmitted from the projection neurons in the BLA (Figure 5e). In future research, the proposed device can not only be used to verify some known neural pathways like pyramidal tracts and dorsal column-medial lemniscus pathway, but also be used to explore some undiscovered pathways that may be potentially significant for complex biological processes.

2.7. Behavior Studies during Optical Stimulation

Experiments to demonstrate the device's capability to conduct wireless behavior regulation on freely moving rats were then performed by the open field test (OFT). The OFT was a 9-minutes session involving three epochs during which the optical stimulation was turned off and on and then off again. *AAV9-CaMKIIα::hChR2-eYFP* was first injected into the mPFC, followed by implanting a flexible channel into the lateral habenula

(LHb), which is a projection target of the mPFC and is related to depression.[38,39] The total traveled distance of rats was suppressed after optical stimulation (Figure 5f; Video S3, Supporting Information) with a 61.14% decrease in the average velocity (Figure 5g), indicating that excitation of the mPFC to LHb projection circuit has a negative effect on rats' exploration behavior in an open field. It was noticed that the rats in the third epoch were not as active as in the initial epoch, possibly because of the prolonged passive recovery periods from the depressed rats. It may also be because that the rats became familiar with the open field environment and unwilling to further explore after previous epochs. The preliminary results of behavior studies suggest great potential to apply the devices on freely moving animals. More complex animal behavior studies with diverse photoreceptors may be conducted in future research to explore the functions to promote excitement or multi-wavelength optical stimulation across different brain regions.

2.8. Assessment of the Long-Term Stability and Biocompatibility

The biocompatibility of the device and its long-term stability were finally explored. Behavior studies of rats implanted with the device show no obvious changes in the traveling distances and the velocities before and after the surgery for two weeks (Figure S17, Supporting Information), indicating that the implantation of multiple channels did not cause locomotion disruption and mental disorder. To evaluate the invasiveness and glial responses, a flexible channel, a commercial optical fiber (polymethyl methacrylate, 250 μm in diameter), and a microwire (gold-modified Tungsten, 100 μm in diameter) were implanted into the brain, and immunohistochemical analysis was performed by quantifying glial response six weeks after surgery. The cross-sectional areas of the channel, the optical fiber, and the microwire were 38 310, 48 490, and 8033 μm^2, respectively (**Figure 6**a–c; Figure S18, Supporting Information).
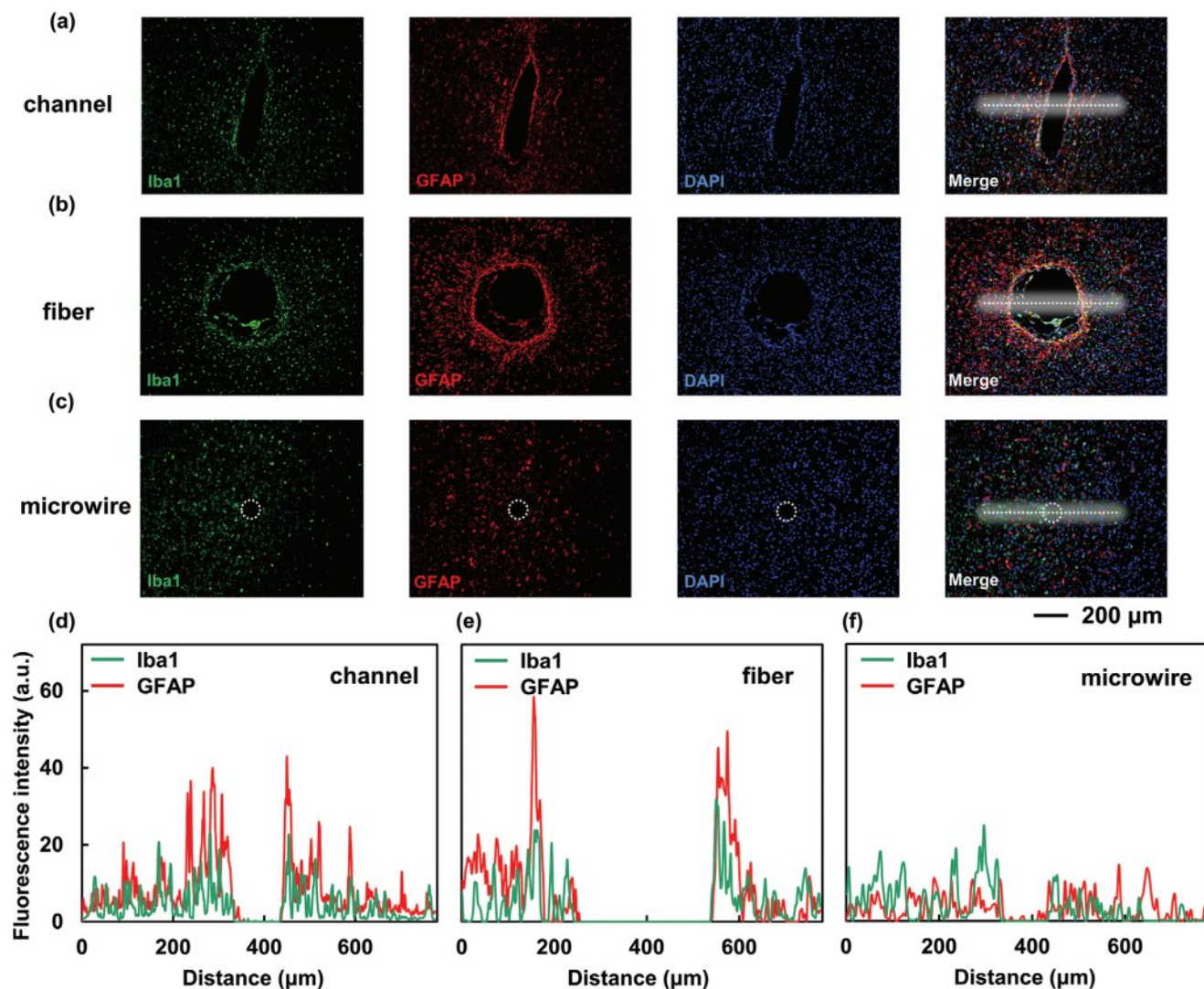

Figure 6. Immunohistochemistry study of different implantable devices. Confocal fluorescence images of 30 μm-thick slices for activated microglia (Iba1, green), astrocytes (GFAP, red), and nuclei (DAPI, blue) at the tips of a) the flexible channel, b) the optical fiber, and c) the microwire, respectively. Representative line plots of averaged fluorescence intensity along the white lines (100 μm in width) at the center of d) the flexible channel, e) the optical fiber, and f) the microwire.

The flexible channel produced less glial activation and lesions as compared to the commercial fiber (Figure 6d,e), which may be attributed to small dimensions of the channel that resulted in reduced tissue damage. However, the positive signal of the astrocytic marker glial fibrillary acidic protein (GFAP) at the periphery of the channel was four times larger than that of the microwire (Figure 6f) due to the relatively large dimension of the channel, which was 4.7 times larger than the microwire. The biocompatibility of the devices depends on the size of the devices and composition materials.[40] Thus, sophisticated complementary metal-oxide-semiconductor (CMOS) fabrication techniques may yield highly integrated systems with miniaturized chips, sensors, and power suppliers, leading to reduced device size and less usage of materials. Some notable examples involve highly integrated CMOS chips for neural interfacing[41–43] and implantable silicon probes for neural activity recording[10,25,44] demonstrated based on rigid CMOS devices. It can be expected that dedicated flexible integrated circuits achieved by controlled spalling,[45,46] mechanical grinding,[47,48] and silicon-on-insulator techniques[49–51] on flexible substrates can lead to smaller device footprints and, thus, better biocompatibility for implantable applications. The chronic functionality of the channels was demonstrated two weeks after implantation. The encapsulated μ-LED within the channel extracted from the brain maintained their function, indicating that the device was well tolerated in freely moving animals (Figure S19, Supporting Information). The results demonstrate that the ultrathin configurations and the flexible mechanics of the device match the soft and curvilinear properties of brain tissues, resulting in enhanced long-term stability and reduced tissue lesion and immunoreactivity.

3. Conclusion

The flexible device contains scattered electronic tentacles that can be modularized to yield functions such as opto-electrical stimulation, biopotential recording, and ion monitoring in multi-encephalic regions with programmable working sequences. It is constructed by various organic and inorganic materials that have been made into thin-film and nanoparticle formats. It can serve as a comprehensive and customizable platform to achieve more sophisticated neural stimulation and biophysiological monitoring to benefit the study of neurological disorders, neuromodulation, and brain mechanisms. Its capability of recording evoked electrical signal and chemical activities under in situ optical or electrical stimulation has been demonstrated. Besides, behavior and immunohistochemistry studies suggest its potential for wireless, long-term regulation of brain functions for freely moving animals.

The device design, materials, and experiments have demonstrated the concept of multi-encephalic modulation. It is possible to achieve even smaller footprints, higher numbers of channels and functional components, and complicated functions by introducing more sophisticated CMOS fabrication techniques and facilities. The comprehensive functions and programmable working sequences of the flexible device have enabled numerous brain-related applications, which will be explored further in our future research. In addition, fully implantable systems may also be achieved by combining state-of-the-art techniques in ultrathin integrated circuits, transcranial wireless power harvesting, and biological fuel cells. It can be expected that fully implantable flexible electronics with multiple electronic tentacles that cover large and different brain regions may eventually be developed to facilitate brain–computer interface, trans-species communication, and in-depth understanding of brain mechanisms.

4. Experimental Section

Preparation of μ-LEDs: GaN-based μ-LEDs (S-08CBAUP-A, San'an Optoelectronics Co., Ltd.) were bonded onto a silicon wafer using a positive photoresist (AZ P4620, Microchem Inc.), followed by laser lift-off using a krypton fluoride (KrF) excimer laser at 248 nm (Ex-power 248, Beijing HLG Instrument Co., Ltd.).[52] The laser energy density was optimized to be around 0.4 J cm^{-2} to thermally decompose GaN into gallium (Ga) and nitrogen at the interface of the μ-LEDs and the sapphire substrate, allowing mechanical removal of the sapphire substrate after heating to 70 °C. The released ultrathin μ-LEDs were then immersed into 5 wt% diluted HCl to remove the Ga residual. After the removal of the photoresist, the released μ-LEDs could be picked up by polydimethylsiloxane (PDMS, Sylgard 184, Dow Corning Corp.) stamps.[53]

Fabrication of the Device: Fabrication of the device started with depositing 500 nm Cu onto a PI film (25 μm in thickness, CHENG LIDA Co., Ltd.) for dissipating heat from the μ-LEDs, which were then transfer-printed onto the Cu layer using UV curable photoresist as an adhesion layer.[54] The μ-LEDs were then encapsulated with SU-8 (8 μm in thickness, SU-8 2005, Microchem Inc.), which was later defined by photolithography to expose vias of μ-LED electrodes and shapes of the channels. Ti/Cu/Ti/Au (5/500/5/50 nm) multilayers were then deposited and patterned to form both the interconnects and the microelectrodes, followed by coating with PI (593052-250ML, Sigma-Aldrich Corp.). Openings with diameters of around 30 μm were formed using reactive ion etching (RIE, CS-1701, Nordson MARCH Inc.) on the microelectrodes, which were later surface-modified with AuNPs through electroplating in an electrolyte solution that contained 0.1 M HAuCl$_4$ and 1 M KCl.[55] The ion-selective sensor was also fabricated through depositing and patterning Ti/Cu/Ti/Au (5/500/5/50 nm) on a PI film (25 μm in thickness). A PI insulation layer was then deposited and patterned by RIE to define the electrode areas. The Ag/AgCl reference electrodes were obtained by plating Ag on the Au reference electrode, followed by immersing the Ag electrode into 50 mM FeCl$_3$ to yield the surface AgCl layer. The PI films that contain the μ-LEDs, the microelectrodes, and the ion-selective sensors could be stacked together using UV curable epoxy (9308, LEAFTOP Co., Ltd.).

Modification of Reference and Ion-Selective Electrodes: A reference solution was prepared by dissolving 791 mg PVB (Shanghai Macklin Biochemical Co., Ltd.), 500 mg NaCl, 20 mg block polymer poly(ethylene oxide)-poly(propylene oxide)-poly(ethylene oxide) (PEO-PPO-PEO, F127, Shanghai Macklin Biochemical Co., Ltd.), and 2 mg multiwall carbon nanotubes into 10 mL methanol.[56] The K$^+$ selective solution was prepared by dissolving 4.2 mg valinomycin (Aladdin Industrial Corp.), 1.1 mg sodium tetrakis[3,5-bis(trifluoromethyl)phenyl] borate (Na-TFPB, Sigma-Aldrich Corp.), 68.6 mg polyvinyl chloride (PVC, Sigma-Aldrich Corp.), and 129.2 mg bis(2-ethylhexyl) sebacate (DOS, Aladdin Industrial Corp.) in 700 μL tetrahydrofuran (THF, Aladdin Industrial Corp.). The Na$^+$ selective solution was prepared by dissolving 2.9 mg Na ionophore X (Sigma-Aldrich Corp.), 1.4 mg Na-TFPB, 84.1 mg PVC, and 167.6 mg DOS in 1780 μL THF. The Ca^{2+} selective solution was prepared by dissolving 3.2 mg calcium ionophore II (ETH 129, Sigma-Aldrich Corp.), 1.5 mg Na-TFPB, 97.9 mg PVC, and 190.3 mg DOS in 1780 μL THF.

The reference electrode was obtained by drop-casting the reference solution (1 μL) onto the Ag/AgCl electrode. Ion-selective electrodes were obtained by drop-casting PEDOT:PSS (1 μL, Sigma-Aldrich

**ADVANCED
SCIENCE NEWS**

www.advancedsciencenews.com

**ADVANCED
FUNCTIONAL
MATERIALS**

www.afm-journal.de

Corp.), followed by drop-casting ion-selective solutions (1 µL) onto corresponding electrodes. All the modified electrodes were left to dry in a dark environment overnight.

Characterization of µ-LEDs and Microelectrodes: Thickness and topography of the released µ-LEDs were measured using a surface profiler (Alpha-Step IQ, KLA Tencor Corp.). Current–voltage characteristics were measured using a source meter (Keithley 2400, Tektronix Inc.). The bending process was performed using a tensile testing machine (ZQ-990B, ZHIQU Precision Instruments Co., Ltd.). The electroluminescent spectra were obtained using a spectrometer (USB2000+, Ocean Optics Inc.). The output power density was measured by a spectroradiometer (HAAS 2000, EVERFINE Corp.) with an integrating sphere. Thermal measurement was performed using a thermal imaging camera (226s, FOTRIC Inc.) with a background temperature of 37 °C. Impedance was measured within a frequency range from 100 Hz to 10 kHz using a precision LCR meter (E4980A, Agilent Technologies Inc.) when immersing sensors into phosphate-buffered saline (PBS, Biological Industries) at room temperature. In vitro microelectrode characterization was performed by immersing four flexible channels into the ACSF with an additional channel connected to a signal generator (DG1062Z, RIGOL Technologies Co., Ltd.) that supplied simulated spikes. The signal measured by the channels was pre-processed by a circuit for filtering and amplification, and recorded by an oscilloscope (DS2072A, RIGOL Technologies Co., Ltd.).

Characterization of Ion-Selective Sensors: In vitro electrochemical measurement was performed using an electrochemical workstation (CHI760E, CH Instrument Inc.). Ion-selective sensors were dipped into a solution containing 0.1 M NaCl, 0.01 M KCl, and 0.01 M $CaCl_2$ for 1 h before the measurement to minimize the drift.[56] The reversibility study was performed by recording the dynamic response under continuous concentration changes from 0.5 to 8, 10 to 160, and 0.25 to 4 mM for K^+, Na^+, and Ca^{2+} sensors, respectively. The selectivity study for Ca^{2+} sensor was performed by adding interferences with physiologically relevant concentrations (0.5 mM Mg^{2+}, 2.5 mM K^+, and 10 mM Na^+) into a base solution (2 mM K^+, 100 mM Na^+, and 1 mM Ca^{2+}).

In Vitro Optogenetic Modulation of Ca^{2+} Activities: The *pcDNA3.1/ChR2-GFP* plasmid was created based on *pcDNA3.1-GFP* provided by Bo Huang (addgene: # 70219),[57] followed by inserting ChR2 (GenBank: EU285660.1) to the N-terminus of GFP. A Ca^{2+} sensor with a transfer-printed µ-LED was bonded to a cell culture plate, followed by treating with poly-L-lysine, culturing with 293T cells for 24 h, and transfecting with *pcDNA3.1/ChR2-GFP* for 48 h. Cells were washed with ACSF for three times and then cultured in ACSF in a 5% CO_2 incubator at 37 °C for 30 min. Cells were then exposed to µ-LED light (1 mA, 120 Hz with a pulse width of 5 ms) for 20 s and relative Ca^{2+} concentration was recorded by measuring the open-circuit potential of the Ca^{2+} sensor.

Virus Injection and Device Implantation: All animal experiments and protocols were approved by the Institute of Radiation Medicine Chinese Academy of Medical Sciences. Sprague Dawley rats (SD, 6–8 weeks) were anesthetized via intraperitoneal injection of pentobarbital sodium (1%, 40 mg kg^{-1} bodyweight), and then positioned in a stereotaxic apparatus (KW-DSY2, Nanjing Calvin Biological Technology Co., Ltd.). The scalps of the rats were incised to expose the skulls. Lambda and bregma points were used to align the skull according to the Rat Brain Atlas.[58] During the process of implantation, each channel of the device was surface-coated with polyvinyl alcohol (PVA) or polyethylene glycol (PEG) to enhance the rigidness of the channel to avoid its bending. Both PVA and PEG could dissolve in the cerebrospinal fluid after implantation to restore the flexibility of the channel. For the multichannel electrophysiological recording, four channels were implanted into the DpG (stereotaxic coordinates from bregma: -5.6 anteroposterior (AP), 1.1 mediolateral (ML), -4.8 mm dorsoventral (DV)), AV (-1.8 AP, 1.6 ML, -4.9 DV), Cpu (1.6 AP, 1.6 ML, -4.8 DV), vHPC (-5.2 AP, 5.3 ML, -5.8 DV), respectively (Figure S20, Supporting Information). For the experiments of projection mapping, *AAV9-CaMKIIα::hChR2-eYFP* virus (BrainVTA(Wuhan) Co., Ltd.) was injected into the BLA (-2.8 AP, 4.9 ML, -8.2 DV) using a microsyringe and an injection pump with a speed of 500 nL min^{-1}. After complete viral expression for one month, flexible channels were then implanted into

the bilateral BLA (-2.8 AP, ±4.9 ML, -8.4 DV) and vHPC (-5.2 AP, 5.3 ML, -5.8 DV). For the optogenetic Ca^{2+} regulation, the virus was delivered into the mPFC (2.7 AP, 0.7 ML, -3.6 DV), followed by implanting the flexible channels after one month. For the open field tests, the virus was delivered into the mPFC (2.2 AP, 0.5 ML, -4.2 DV) then channels were implanted into the LHb (-3.6 AP, 0.8 ML, -4.6 DV), and connected to a wireless circuit (Figure S3, Supporting Information) fixed to the skull using dental cement. Rats were allowed to recover for at least one month. For the immunohistochemistry study, a flexible channel, an optical fiber (polymethyl methacrylate, 250 µm in diameter, Shenzhen Qi Yi POF Co., Ltd.), and a microwire (gold-modified Tungsten, 100 µm in diameter, Kedou Brain-Computer Technology Co., Ltd.) were implanted to the HPC (-3.2 AP, ± 2.0 ML, -3.6 DV). The rats were allowed to recover for six weeks before the immunohistochemical analysis.

In Vivo Electrophysiological Recording and Projection Mapping: Channels implanted in the brain were connected to a battery-powered circuit or a commercial neural recording data acquisition system (Omniplex, Plexon Inc.). Light stimulation (2.6 V, 500-ms pulse width, ≈6.5 mW mm^{-2}) was performed wirelessly to excite the neurons. Signal was band-pass filtered between 0.1–300 Hz for LFP analysis or between 500–5000 Hz for spikes. Spikes were sorted using principal component analysis (Offline Sorter, Plexon Inc.). Interspike interval and power spectral density were analyzed by a data analysis software (NeuroExplorer, Nex Technologies).

In Vivo Optogenetic Modulation of Ca^{2+} Activities: Flexible channels implanted in the mPFC were connected to a wireless circuit for optical stimulation and Ca^{2+} monitoring. Light stimulation (2.6 V, 120 Hz with a pulse width of 5 ms) was conducted in the mPFC, while the corresponding Ca^{2+} concentrations were measured through the open-circuit potential of the Ca^{2+} sensors.

Open Field Tests: OFTs were performed with SD rats transfected with *AAV9-CaMKIIα::hChR2-eYFP* in the mPFC. All trials (9-min session, 3-min OFF/ON/OFF epochs, 20 Hz, 5-ms pulse width) were recorded by a video camera, and locomotor activity was analyzed with a video tracking software (SMART, Panlab Inc.).

Immunohistochemistry and Imaging: Rats were anesthetized with pentobarbital sodium and intracardially perfused with 4% paraformaldehyde in PBS. Brains were dissected, fixed for 24 h at 4 °C, and cryoprotected with a 30% sucrose solution in 0.1 M PBS at 4 °C for 24 h. Brains were then cut into slices (30 µm in thickness) that were then washed three times in PBS and blocked in blocking buffer (PBS containing 0.5% Triton X-100 and 3% bovine serum albumin) for 1 h at room temperature. Brain slices were then incubated for 12 h at 4 °C in blocking buffer that contained rabbit anti-Iba1 (ab178846, Abcam Inc., 1:200) and mouse anti-GFAP (60190-1-lg, Proteintech Inc., 1:500). Then slices were washed three times in PBS and incubated for 1 h at room temperature in blocking buffer that contained Alexa Fluor 488 goat anti-rabbit IgG (bs-0295G-AF488, Bioss Inc., 1:200) and Alexa Fluor 555 goat anti-mouse IgG (bs-0296G-AF555, Bioss Inc., 1:200). Afterward, slices were washed three times in PBS and then incubated with 4′,6-diamidino-2-phenylindole (DAPI, AR1176, Boster Biological Technology Co., Ltd.) in 0.1 M PBS that also contained 3% bovine serum albumin for 1 h at room temperature. After being washed three times in PBS, brain slices were mounted on glass slides with 50% glycerin. All slices were imaged on a confocal microscope (A1 HD25, Nikon Corp.). The fluorescence intensity was analyzed using the line profile function of ImageJ.

Supporting Information

Supporting Information is available from the Wiley Online Library or from the author.

Acknowledgements

[1] J. E. LeDoux, *The Emotional Brain: The Mysterious Underpinnings of Emotional Life*, Simon & Schuster, New York **1996**.

[2] E. Oja, *Int. J. Neural Syst.* **1989**, *01*, 61.

[3] S. k. Schultz, *Am. J. Psychiatry* **2001**, *158*, 662.

[4] S. B. Laughlin, T. J. Sejnowski, *Science* **2003**, *301*, 1870.

[5] O. Sporns, D. R. Chialvo, M. Kaiser, C. C. Hilgetag, *Trends Cognit. Sci.* **2004**, *8*, 418.

[6] J. K. Rilling, M. F. Glasser, T. M. Preuss, X. Ma, T. Zhao, X. Hu, T. E. Behrens, *Nat. Neurosci.* **2008**, *11*, 426.

[7] J. J. Gooley, J. Lu, T. C. Chou, T. E. Scammell, C. B. Saper, *Nat. Neurosci.* **2001**, *4*, 1165.

[8] F. Wu, E. Stark, P. C. Ku, K. D. Wise, G. Buzsaki, E. Yoon, *Neuron* **2015**, *88*, 1136.

[9] K. Kampasi, D. F. English, J. Seymour, E. Stark, S. McKenzie, M. Vöröslakos, G. Buzsáki, K. D. Wise, E. Yoon, *Microsyst. Nanoeng.* **2018**, *4*, 10.

[10] H. Shin, Y. Son, U. Chae, J. Kim, N. Choi, H. J. Lee, J. Woo, Y. Cho, S. H. Yang, C. J. Lee, I.-J. Cho, *Nat. Commun.* **2019**, *10*, 3777.

[11] D. Schwarz, M. Kollo, C. Bosch, C. Feinauer, I. Whiteley, T. W. Margrie, T. Cutforth, A. T. Schaefer, *Nat. Commun.* **2018**, *9*, 183.

[12] D. L. Hunt, C. Lai, R. D. Smith, A. K. Lee, T. D. Harris, M. Barbic, *Nat. Biomed. Eng.* **2019**, *3*, 741.

[13] T. Bullmann, M. Radivojevic, S. T. Huber, K. Deligkaris, A. Hierlemann, U. Frey, *Front. Cell. Neurosci.* **2019**, *13*, 404.

[14] G. Charvet, L. Rousseau, O. Billoint, S. Gharbi, J. P. Rostaing, S. Joucla, M. Trevisiol, A. Bourgerette, P. Chauvet, C. Moulin, F. Goy, B. Mercier, M. Colin, S. Spirkovitch, H. Fanet, P. Meyrand, R. Guillemaud, B. Yvert, *Biosens. Bioelectron.* **2010**, *25*, 1889.

[15] K. N. Noh, S. I. Park, R. Qazi, Z. Zou, A. D. Mickle, J. G. Grajales-Reyes, K. I. Jang, R. W. t. Gereau, J. Xiao, J. A. Rogers, J. W. Jeong, *Small* **2018**, *14*, 1702479.

[16] Y. Zhang, D. C. Castro, Y. Han, Y. Wu, H. Guo, Z. Weng, Y. Xue, J. Ausra, X. Wang, R. Li, G. Wu, A. Vazquez-Guardado, Y. Xie, Z. Xie, D. Ostojich, D. Peng, R. Sun, B. Wang, Y. Yu, J. P. Leshock, S. Qu, C. J. Su, W. Shen, T. Hang, A. Banks, Y. Huang, J. Radulovic, P. Gutruf, M. R. Bruchas, J. A. Rogers, *Proc. Natl. Acad. Sci. U.S.A.* **2019**, *116*, 21427.

[17] W. Bai, J. Shin, R. Fu, I. Kandela, D. Lu, X. Ni, Y. Park, Z. Liu, T. Hang, D. Wu, Y. Liu, C. R. Haney, I. Stepien, Q. Yang, J. Zhao, K. R. Nandoliya, H. Zhang, X. Sheng, L. Yin, K. MacRenaris, A. Brikha, F. Aird, M. Pezhouh, J. Hornick, W. Zhou, J. A. Rogers, *Nat. Biomed. Eng.* **2019**, *3*, 644.

[18] J. Shin, Z. Liu, W. Bai, Y. Liu, Y. Yan, Y. Xue, I. Kandela, M. Pezhouh, M. R. MacEwan, Y. Huang, W. Z. Ray, W. Zhou, J. A. Rogers, *Sci. Adv.* **2019**, *5*, eaaw1899.

[19] T.-M. Fu, G. Hong, R. D. Viveros, T. Zhou, C. M. Lieber, *Proc. Natl. Acad. Sci. U. S. A.* **2017**, *114*, E10046.

[20] X. Yang, T. Zhou, T. J. Zwang, G. Hong, Y. Zhao, R. D. Viveros, T. M. Fu, T. Gao, C. M. Lieber, *Nat. Mater.* **2019**, *18*, 510.

[21] G. Hong, X. Yang, T. Zhou, C. M. Lieber, *Curr. Opin. Neurobiol.* **2018**, *50*, 33.

[22] E. S. Boyden, F. Zhang, E. Bamberg, G. Nagel, K. Deisseroth, *Nat. Neurosci.* **2005**, *8*, 1263.

[23] K. Deisseroth, *Nat. Methods* **2011**, *8*, 26.

[24] W. M. Grill, A. N. Snyder, S. Miocinovic, *Neuroreport* **2004**, *15*, 1137.

[25] A. Mohanty, Q. Li, M. A. Tadayon, S. P. Roberts, G. R. Bhatt, E. Shim, X. Ji, J. Cardenas, S. A. Miller, A. Kepecs, M. Lipson, *Nat. Biomed. Eng.* **2020**, *4*, 223.

[26] J. T. Coull, *Prog. Neurobiol.* **1998**, *55*, 343.

[27] D. L. Robinson, A. Hermans, A. T. Seipel, R. M. Wightman, *Chem. Rev.* **2008**, *108*, 2554.

[28] W. Ling, G. Liew, Y. Li, Y. Hao, H. Pan, H. Wang, B. Ning, H. Xu, X. Huang, *Adv. Mater.* **2018**, *30*, 1800917.

[29] K. Deisseroth, *Nat. Neurosci.* **2015**, *18*, 1213.

[30] T. Kushibiki, S. Okawa, T. Hirasawa, M. Ishihara, *Int. J. Photoenergy* **2014**, *2014*, 895039.

[31] K. M. Tye, K. Deisseroth, *Nat. Rev. Neurosci.* **2012**, *13*, 251.

[32] S. K. Mohanty, I. P. Clements, N. V. Thakor, A. G. Gnade, A. D. Rush, C. D. Patten, M. C. Twomey, A. V. Kravitz, in *Optogenetics: Optical Methods for Cellular Control*, Vol. 14, SPIE, San Francisco, CA **2013**.

[33] R. Kim, N. Hong, Y. Nam, *Biotechnol. J.* **2013**, *8*, 206.

[34] S. Luan, I. Williams, K. Nikolic, T. G. Constandinou, *Front. Neuroeng.* **2014**, *7*, 27.

[35] R. di Terlizzi, S. Platt, *Vet. J.* **2006**, *172*, 422.

[36] M. J. Berridge, M. D. Bootman, H. L. Roderick, *Nat. Rev. Mol. Cell Biol.* **2003**, *4*, 517.

[37] A. C. Felix-Ortiz, K. M. Tye, *J. Neurosci.* **2014**, *34*, 586.

[38] M. R. Warden, A. Selimbeyoglu, J. J. Mirzabekov, M. Lo, K. R. Thompson, S. Y. Kim, A. Adhikari, K. M. Tye, L. M. Frank, K. Deisseroth, *Nature* **2012**, *492*, 428.

[39] M. Matsumoto, O. Hikosaka, *Nat. Neurosci.* **2009**, *12*, 77.

[40] J. P. Seymour, F. Wu, K. D. Wise, E. Yoon, *Microsyst. Nanoeng.* **2017**, *3*, 16066.

[41] A. Hierlemann, J. Muller, D. Bakkum, F. Franke, in *Technical Digest IEEE Int. Electron Devices Meeting (IEDM)*, IEEE, Washington, USA **2015**, p. 13.2.1.

[42] B. Miccoli, C. M. Lopez, E. Goikoetxea, J. Putzeys, M. Sekeri, O. Krylychkina, S. W. Chang, A. Firrincieli, A. Andrei, V. Reumers, D. Braeken, *Front. Neurosci.* **2019**, *13*, 641.

[43] A. Obaid, M.-E. Hanna, Y.-W. Wu, M. Kollo, R. Racz, M. R. Angle, J. Müller, N. Brackbill, W. Wray, F. Franke, E. J. Chichilnisky, A. Hierlemann, J. B. Ding, A. T. Schaefer, N. A. Melosh, *Sci. Adv.* **2020**, *6*, eaay2789.

[44] J. J. Jun, N. A. Steinmetz, J. H. Siegle, D. J. Denman, M. Bauza, B. Barbarits, A. K. Lee, C. A. Anastassiou, A. Andrei, Ç. Aydın, M. Barbic, T. J. Blanche, V. Bonin, J. Couto, B. Dutta, S. L. Gratiy, D. A. Gutnisky, M. Häusser, B. Karsh, P. Ledochowitsch, C. M. Lopez, C. Mitelut, S. Musa, M. Okun, M. Pachitariu, J. Putzeys, P. D. Rich, C. Rossant, W.-l. Sun, K. Svoboda, M. Carandini, K. D. Harris, C. Koch, J. O'Keefe, T. D. Harris, *Nature* **2017**, *551*, 232.

[45] D. Shahrjerdi, S. W. Bedell, *Nano Lett.* **2013**, *13*, 315.

[46] N. Li, S. Bedell, H. Hu, S. J. Han, X. H. Liu, K. Saenger, D. Sadana, *Adv. Mater.* **2017**, *29*, 1606638.

[47] A. Vilouras, H. Heidari, S. Gupta, R. Dahiya, *IEEE Trans. Electron Devices* **2017**, *64*, 2038.

[48] S. Gupta, W. T. Navaraj, L. Lorenzelli, R. Dahiya, *npj Flexible Electron.* **2018**, *2*, 8.

[49] B. Chen, H. Wu, C. Xin, D. Dai, L. Tong, *Nat. Commun.* **2017**, *8*, 20.

[50] W. T. Navaraj, S. Gupta, L. Lorenzelli, R. Dahiya, *Adv. Electron. Mater.* **2018**, *4*, 1700277.

[51] E. Song, C.-H. Chiang, R. Li, X. Jin, J. Zhao, M. Hill, Y. Xia, L. Li, Y. Huang, S. M. Won, K. J. Yu, X. Sheng, H. Fang, M. A. Alam, Y. Huang, J. Viventi, J.-K. Chang, J. A. Rogers, *Proc. Natl. Acad. Sci. U. S. A.* **2019**, *116*, 15398.

[52] W. S. Wong, T. Sands, N. W. Cheung, M. Kneissl, D. P. Bour, P. Mei, L. T. Romano, N. M. Johnson, *Appl. Phys. Lett.* **1999**, *75*, 1360.

[53] T. I. Kim, J. G. McCall, Y. H. Jung, X. Huang, E. R. Siuda, Y. Li, J. Song, Y. M. Song, H. A. Pao, R. H. Kim, C. Lu, S. D. Lee, I. S. Song, G. Shin, R. Al-Hasani, S. Kim, M. P. Tan, Y. Huang, F. G. Omenetto, J. A. Rogers, M. R. Bruchas, *Science* **2013**, *340*, 211.

[54] T.-i. Kim, M. J. Kim, Y. H. Jung, H. Jang, C. Dagdeviren, H. A. Pao, S. J. Cho, A. Carlson, K. J. Yu, A. Ameen, H.-j. Chung, S. H. Jin, Z. Ma, J. A. Rogers, *Chem. Mater.* **2014**, *26*, 3502.

[55] H. du Toit, M. di Lorenzo, *Sens. Actuators, B* **2014**, *192*, 725.

[56] W. Gao, S. Emaminejad, H. Y. Y. Nyein, S. Challa, K. Chen, A. Peck, H. M. Fahad, H. Ota, H. Shiraki, D. Kiriya, D.-H. Lien, G. A. Brooks, R. W. Davis, A. Javey, *Nature* **2016**, *529*, 509.

[57] D. Kamiyama, S. Sekine, B. Barsi-Rhyne, J. Hu, B. Chen, L. A. Gilbert, H. Ishikawa, M. D. Leonetti, W. F. Marshall, J. S. Weissman, B. Huang, *Nat. Commun.* **2016**, *7*, 11046.

[58] G. Paxinos, C. Watson, *The Rat Brain in Stereotaxic Coordinates: Hard Cover Edition*, Academic Press, San Diego, CA **2006**.